

Confinement analyses of the high-density field-reversed configuration plasma in the field-reversed configuration experiment with a liner

Shouyin Zhang,^{a)} T. P. Intrator, G. A. Wurden, W. J. Waganaar,
J. M. Taccetti, and R. Renneke
Los Alamos National Laboratory, Los Alamos, New Mexico 87545

C. Grabowski
Science Applications International Corporation, Albuquerque, New Mexico 87106

E. L. Ruden
Air Force Research Laboratory, Albuquerque, New Mexico 87117

(Received 9 December 2004; accepted 8 March 2005; published online 5 May 2005)

The focus of the field-reversed configuration (FRC) experiment with a liner (FRX-L) is the formation of a target FRC plasma for magnetized target fusion experiments. An FRC plasma with density of 10^{23} m^{-3} , total temperature in the range of 150–300 eV, and a lifetime of $\approx 20 \mu\text{s}$ is desired. Field-reversed θ -pinch technology is used with programed cusp fields at θ -coil ends to achieve non-tearing field line reconnections during FRC formation. Well-formed FRCs with density between $(2\text{--}4) \times 10^{22} \text{ m}^{-3}$, lifetime in the range of 15–20 μs , and total temperature between 300–500 eV are reproducibly created. Key FRC parameters have standard deviation in the mean of 10% during consecutive shots. The FRCs are formed at 50 mTorr deuterium static fill using 2 kG net reversed bias field inside the θ -coil confinement region, with external main field unexpectedly ranging between 15–30 kG. The high-density FRCs confinement properties are approximately in agreement with empirical scaling laws obtained from previous experiments with fill pressure mostly less than 20 mTorr. Analyses in this paper reveal that reducing the external main field modulation and/or extending the θ -coil length in the FRX-L device are critical in achieving higher FRC parameters for application in magnetized target fusion. © 2005 American Institute of Physics. [DOI: 10.1063/1.1899648]

I. INTRODUCTION

Magnetized target fusion^{1,2} (MTF) is an alternate fusion energy concept intermediate in density and lifetime to usual magnetic fusion energy³ (MFE) and inertial confinement fusion⁴ (ICF) schemes, but which combines features of both. MTF uses a magnetized plasma compressed by an external flux conserving shell or “pusher,” so compression is inertial as in ICF, while thermal insulation is magnetic as in MFE. Advantages of this concept include lower system cost due to a significantly increased compression time scale relative to ICF (easily achievable by existing pulsed power systems), and a much smaller system size relative to MFE. A variety of plasmas might be suitable for a target, and there are also a number of compression concepts and methodologies to compress the plasma.^{5,6} We have chosen the field-reversed configuration (FRC) plasma as the target plasma along with a solid cylindrical liner (pusher) to adiabatically compress the FRC in the FRC-MTF scheme at Los Alamos National Laboratory. The reasons for the choice are discussed elsewhere.^{1,2,7,8}

An FRC formed by traditional field-reversed θ -pinch (FRTP) (Ref. 9) method is sketched in Fig. 1. The FRC plasma is enclosed inside a separatrix volume. External magnetic field pressure of open-field lines outside the separatrix balances plasma pressure in the radial direction; closed-field

line tension or curvature force balances the particle pressure at the ends (axial direction). Inside the separatrix, closed magnetic field lines (trapped flux) are embedded in the compact plasma toroid. This closed-field-line topology makes the FRC robust during translation¹⁰ and hopefully during compression. An FRC naturally exhibits two prominent features: the plasma β is close to unity, and the open-field lines at θ -coil ends act as divertors to potentially divert the influx of impurities from plasma-wall interactions. FRC has been investigated for decades since the 1960s, and the experimental results up to 1988 were reviewed by Tuszewski.¹¹

The approach to the FRC-MTF scheme includes optimization of the triple product $nT\tau$, which is a different focus compared to other present FRC experiments.^{12–15} The first objective in the scheme is to produce FRC plasma with density of 10^{23} m^{-3} , total temperature in the range of 150–300 eV, and a lifetime of $\approx 20 \mu\text{s}$ as a target plasma for MTF. Although none of these individual parameters of the target FRC for MTF is a historic achievement compared to previous FRC experiments,¹¹ the requirement to produce such an FRC plasma with each parameter in the desired range is quite a challenge. Especially, the FRC must be highly reproducible so that further translation into a liner region and subsequent compression does not occur for a badly formed target or no target plasma at all. After considering the several available FRC formation techniques,¹¹ we concluded that the FRTP method is the most promising one and historically

^{a)}Electronic mail: sy_zhang66@hotmail.com

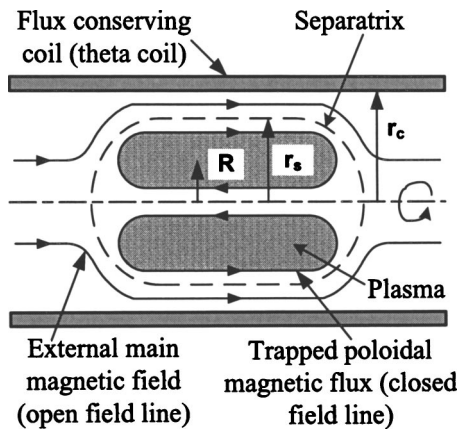


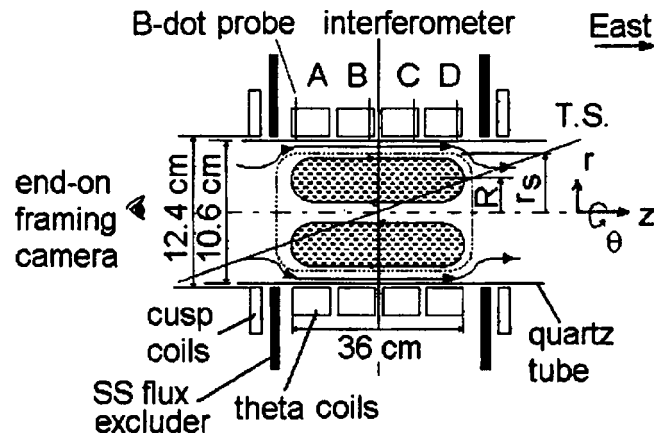
FIG. 1. The geometry of FRC by FRTP formation technique.

demonstrated the ability to form clean low Z_{eff} FRC plasmas in a similar density range as desired for an MTF target plasma (refer to Table II of Ref. 11). However, optimal FRC formation is always a trial-and-error process in each specific device, and some empirical procedures must be formulated to get reproducible FRC plasmas.^{11,12,16}

The existing FRC scaling laws such as FRC stable time,¹⁷⁻¹⁹ flux retention, particle inventory, and energy confinement^{12,13,20-22} as well as heating¹⁶ due to flux annihilation were obtained from experimental data at low fill pressures (typically fill pressure $P_0 < 20$ mTorr, yielding $n_e \sim 10^{20}-10^{21} \text{ m}^{-3}$), yet the target FRC plasma density in MTF is desired to be 10^{23} m^{-3} . Such high-density FRCs are very collisional compared to all previous experiments.²³ Therefore, the extrapolation of the empirical laws into the high-density FRC regime has to be verified. The situation will be more uncertain when the FRC is further compressed in the MTF scheme.

FRC stability in the high-density regime is another issue. It has been found that FRC stability and transport behavior are related to the FRC size parameter S^* , FRC elongation E , and their ratio S^*/E , where S^* is the number of ion skin depths evaluated at volume averaged density inside the separatrix radius²⁰ (S^* is approximately related with small s by $S^* \sim 10s$, where small s is defined as the ratio of FRC radial scale length to the ion gyroradius at the separatrix^{12,13}), and E is the ratio of FRC separatrix length over twice the separatrix radius.^{11-13,16,20,22,24,25} However, the exact stability boundaries have not been identified. The field-reversed configuration experiment with a liner (FRX-L) experiments provide a real case of FRC formation in the $10^{22} \text{ m}^{-3}-10^{23} \text{ m}^{-3}$ density regime with well diagnosed data to compare with previous experiments and theoretical work.

In this paper, optimum well-formed FRC plasmas with high electron density of $(2-4) \times 10^{22} \text{ m}^{-3}$, total temperature of 300–500 eV, and lifetime of 15–20 μs are analyzed to compare with previous empirical scaling laws. The achieved FRC density is within a factor of 2–3 from the desired density in FRC-MTF scheme, the FRC stable time is half the desired value, and the temperature is in the desired range for the MTF target plasma. In Sec. II, the experimental device and the diagnostics are briefly described; in Sec. III, typical

FIG. 2. A cutaway view of FRX-L. The θ -coil length and diameter, the quartz tube diameter, θ -coil segments, cusp coils, and excluded flux plates are shown; some of the important diagnostics are also shown.

FRC shots are analyzed in detail to reveal current FRC confinement properties and problems; and in Sec. IV, statistics are presented to show how well we can reproduce the illustrated high-density FRC, which establishes confidence on using FRC as the target plasma for MTF. The paper concludes with summary and brief discussions.

II. EXPERIMENTAL FACILITY AND DIAGNOSTICS

FRX-L is designed to form, confine, and translate the target FRC plasma.²⁶ As shown in Fig. 2, FRX-L has a quartz tube vacuum chamber with internal diameter of 10.6 cm and a length of 100 cm. The tube is surrounded by an aluminum single turn coil (θ -coil) with internal diameter of 12.6 cm and total length of $l_c = 36$ cm. The coil is segmented into four sections providing three 1 cm slots between coil segments for the accessibility of side-on diagnostics. Bias field bank, preionization (PI) ringing field bank, and main field bank are connected in parallel to the θ -coil. A pair of cusp/mirror coils sits at both ends of θ -coil with stainless steel plates (SS flux excluder) between the θ -coil and cusp coils. The bias field, PI field, main field, cusp field, and the plates define the magnetic configuration at the θ -coil ends and determine net soaked bias field B_0 inside the θ -coil region, which affects FRC formation.

Diagnostic challenges on FRX-L are unique, because of the high-density, short time scale FRC plasma, the strong-pulsed electromagnetic environment around the compact-sized device, and the restricted access to the plasma.²⁷ As shown in Fig. 2, the four segments of θ -coil are labeled as A, B, C, and D from west to east. Magnetic field pick-up probes (B-dots) are inserted from the top through 4.6 mm diameter holes, touching the tube outer wall to measure the local axial magnetic field. A total of 16 probes along the axial direction gives 2 cm axial resolution in excluded flux radius profile measurements.²⁸ An eight-channel helium-neon ($\lambda = 632.8 \text{ nm}$) laser interferometer looks through half of the tube cross section at midplane, measuring the line integrated densities at the following impact parameter radii: $r = 0 \text{ cm}$, 0.7 cm, 1.9 cm, 2.4 cm, 3.0 cm, 3.4 cm, 3.6 cm, and 4.2 cm. Side-on optical arrays, optical multi channel analyzer

TABLE I. Basic diagnostics in FRX-L.

Diagnostics description	Installation	Measured and deduced plasma parameters
Laser interferometer (He-Ne), $\lambda=632.8$ nm	Eight channels; impact parameters at 0, 0.7, 1.9, 2.4, 3.0, 3.4, 3.6, and 4.2 cm; Abel inversion for density radial profile ready	Eight line integrated densities; $\langle\beta\rangle$, particle retention, τ_N ; FRC stable time τ_s
Local axial external magnetic fields, magnetic fluxes	16 axial magnetic probes spaced 2 cm apart; four flux loops at each θ -coil section	$B_e(z)$, r_s , x_s , $\langle\beta\rangle$, τ_Φ , FRC volume, particle retention, τ_p
Two-dimensional magnetic field mapping	Three pairs of radial and axial probes at θ -coil ends located in the slots among θ -coil end, excluded flux plate, and cusp coil	Tracking cusp point locations at θ -coil ends during FRC formation
Plasma impurity monitoring	Optical multichannel analyzer (OMA) spectroscopy viewing plasma through end-on on-axis and side-on centerline, gated, or continuous mode, 400–700 nm	Characteristic spectral lines of impurities (O, Si, C), indication of impurity varieties and contents
Temporal evolution of impurity line	DIGIKROM 240	Time history of impurity line
Plasma macrodynamics	Framing camera IMACON 775; end-on, 8 frames, 1 μ s interval, 0.2 μ s exposure	Plasma asymmetry, macroinstability
Plasma macroinstability	Two optical array fans, each consists of 8 channels. Visible light intensity	FRC shape, instability, and movement
Multipoint Thomson scattering system	Two to six locations along z axis.	$T_e(r, t, z)$

spectrometers (OMA), and various monochromators are fed via optic fibers accessing through either slots between θ -coil segments or holes on the θ -coil segments. The basic diagnostics on FRX-L are summarized in Table I.

The axial profile of separatrix radii r_s of an FRC is approximated by the measured excluded flux radius (Ref. 29), $r_s \approx r_{\Delta\Phi} = (-\Delta\Phi / \pi B_e)^{1/2}$, where $\Delta\Phi$ and B_e are directly measured by flux loops and local magnetic probes. The volume average beta $\langle\beta\rangle$ is then derived by $\langle\beta\rangle = 1 - x_s^2/2$, $x_s = r_s/r_c$, where r_c is the θ -coil inner radius.¹¹ An estimation of total FRC temperature is based on the FRC radial pressure equilibrium $n(T_e + T_i) = \langle\beta\rangle B_e^2 / 2\mu_0$, where $n = \int n dr / 2r_s$ is volume averaged density, i.e., the center chord-line-density divided by twice the separatrix radius r_s .

III. TYPICAL HIGH-DENSITY FRC PLASMA IN FRX-L

A. Evolution of FRC basic parameters

Figure 3 shows the time histories of typical high-density FRC plasma parameters at 50 mTorr deuterium static fill in FRX-L. The net reversed bias field B_0 is about 2 kG by the time when the main field is switched on at 24.1 μ s. Key plasma parameters are summarized in Table II. At 30 μ s, which is 5 μ s after FRC formation, and during the middle of the FRC equilibrium, the average volume density is 2×10^{22} m⁻³, total temperature is 270 eV, and internal poloidal flux trapped in FRC is about 0.5 mWb, when estimated by $\Phi_p = \pi r_c^2 B_e (x_s/\sqrt{2})^{3+\varepsilon}$, taking $\varepsilon=0.25$ consistent with FRX-series data.^{10,18,23} These numbers represent the present capability for FRX-L to produce and confine an FRC plasma.

Due to the large inductance in the transmission line (including crowbar rail-gap switches), the crowbarred main field experiences strong ringing, which trims the FRC plasma performance in FRX-L all the time. As shown in Fig. 3(e), the modulation is as high as $(B_M - B_m)/(B_M - B_0) \sim 50\%$, where B_M is the peak field in the first cycle after the main field is switched on and B_m is the minimum in the first cycle. The FRC performance can easily be distinguished into three stages in the equilibrium: the approximate

1 μ s (26.5–27.6 μ s) plateau immediately after the FRC is formed, the middle of the equilibrium, and the development of $n=2$ rotational instability. The FRC has high parameters immediately after its formation: electron density maintains at about 4×10^{22} m⁻³ and total temperature reaches about 550 eV. These are almost twice the values measured during the middle of the equilibrium around 30 μ s.

B. FRC dimensions and particle confinement

Time evolution of half the separatrix length l_s is shown in Fig. 4(b). l_s is defined as the length from the end-to-end of the FRC separatrix volume when $r_{\Delta\Phi}$ decreases from maxi-

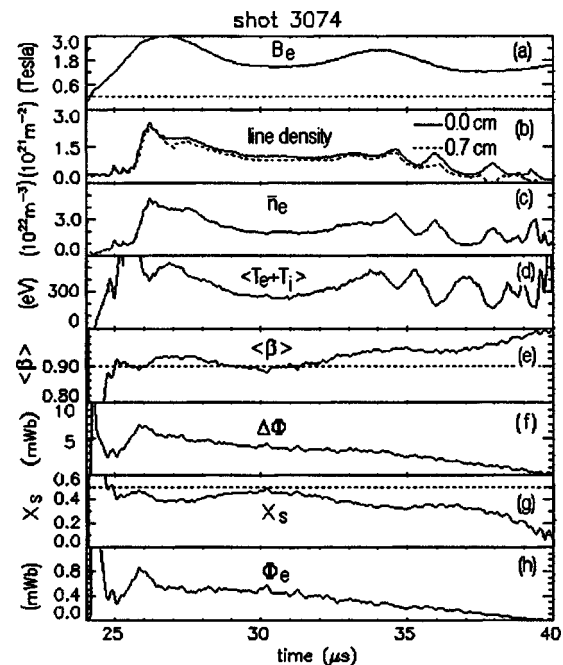


FIG. 3. Temporal evolutions of FRC parameters. (a) External field measured at midplane, (b) line density at center chord (solid line) and off-center chord with impact parameter of 0.7 cm (dashed line), (c) volume average density, (d) total temperature, (e) volume average β , (f) excluded flux measured at midplane, (g) normalized separatrix radius at midplane, and (h) estimated trapped poloidal flux in FRC.

TABLE II. Key FRC parameters in typical FRC shot in FRX-L.

Key FRC parameters	At 26.5 μ s	At 30 μ s
Volume density (10^{22} m $^{-3}$)	4	2
Total temperature (eV)	550	270
Average β	0.92	0.90
X_s	0.38	0.45
Ploidal flux (mWb)	0.55	0.50
External field (kG)	30	15

imum at midplane to $r_{\Delta\Phi} \sim 1$ cm at each end. We choose the 1 cm truncation value because $r_{\Delta\Phi}$ is bigger than r_s at the ends of an FRC plasma,²⁹ and increased error arises from noise in excluded flux measurements when calculating $r_{\Delta\Phi}$ at FRC ends. This truncation may lead to underestimation of FRC plasma volume and particle inventory compared to the definitions adopted by Steinhauer.³⁰ Also shown in Fig. 4(b), the axial location and movement of the centroid of the FRC is indicated by comparing the displacements of FRC ends from geometric center $z=0$. In shot 3074, the FRC center was about 0.7 cm west from θ -coil midplane initially and drifted to ~ 1.7 cm west of $z=0$ at the middle of equilibrium phase. The center moved toward the west end of the θ -coil at a speed of ~ 0.6 cm/ μ s, which is several percent of the local Alfvén velocity. In poorly formed FRC shots, FRCs often

escaped from either ends of the θ -coil at speed up to $\sim 10\%$ of the Alfvén velocity. FRC elongation E changes from 2.9 immediately after axial contraction to 3.6 when the FRC expands to maximum volume due to B_e decreasing as a result of ringing of the main field.

The FRC separatrix volume $V_{\text{FRC}} = \int l_s d(\pi r_s^2)$ in shot 3074 is 2.0×10^{-4} m 3 at 27 μ s and 3.7×10^{-4} m 3 at 30 μ s. They are 6% and 11%, respectively, of the cylindrical volume confined by the θ -coil sections. Early experiments such as LSX,¹² TRX-2, and FRX-C,³¹ had ratios between 7%–18 % with fill pressures below 10 mTorr. The FRC particle inventory [Fig. 4(d)] is subsequently estimated by $N_p = V_{\text{FRC}} \int n dr / 2r_s$, where the integral is the center chord-line-density measured by side-on interferometry at the midplane ($z=0$). The FRC particle inventory just after axial contraction is 8.9×10^{18} , which indicates that 85% of the total particles contained inside the quartz tube in the length of θ -coil l_c are trapped. Previous experiments showed fractions ranging between 35%–100%.^{30,31} Here the FRC volume is calculated based on real time excluded flux radii axial profiles.

It is obvious in Fig. 4(d) that the good particle confinement was maintained between 26.5–30.5 μ s and deteriorated significantly when B_e increased again from minimum due to ringing. Defining particle confinement time (lifetime) as $\tau_N = -N_p / (dN_p / dt)$,^{20,22} we obtain $\tau_N \approx 40$ μ s during 26.5–30.5 μ s and $\tau_N \approx 16$ μ s afterwards. Since the observation time is shorter than the particle lifetime, an estimate of error of $\pm 10\%$ can arise in obtaining the confinement time when adjusting the time range in the exponential fitting procedure; this is also true in the process of obtaining flux confinement time in the following discussions. However, it will be shown in Sec. IV that most FRC parameters can be reproduced with standard deviations in the mean of less than 10%, when consecutive shots were discharged in a restricted optimum operational parameter window to form the typical FRCs such as shown in Fig. 3. This implies that the analyses performed here in one typical shot can appropriately represent the set of well formed FRCs at 50 mTorr in FRX-L. As shown in Fig. 5, the obtained particle confinement time $\tau_N \approx 40$ μ s during 26.5–30.5 μ s in the shot is plotted into the Fig. 8 of Ref. 12. The value is slightly above the fitting curve (empirical scaling),¹² while the value $\tau_N \approx 16$ μ s is much lower than the fitting curve when external field starts increasing again.

C. FRC flux trapping and confinement properties

The FRC shown in Fig. 3 also has good initial flux trapping and retention efficiency. Lift-off field B_{LO} is estimated during the radial compression phase by excluded flux measurements [Fig. 3(g)].¹⁶ $B_{\text{LO}} \approx \Delta\Phi_a / (2\pi r_w^2) \approx 1.7$ kG, where $\Delta\Phi_a$ is the average of excluded flux during the radial compression phase and $r_w = 5.32$ cm is the quartz tube inner radius. B_{LO} is about 84% of the applied net bias $B_0 \approx 2$ kG in the shot. The final flux retention factor $\Phi_e / \Phi_{\text{LO}} \approx 0.33$ is in very good agreement with empirical scaling $\Phi_e / \Phi_{\text{LO}} = 0.85 r_w (\text{cm}) P_0^{1/2} (\text{mTorr})$, where Φ_e is an equilibrium value of the trapped internal flux and $\Phi_{\text{LO}} = B_{\text{LO}} (\pi r_w^2)$ is the lift-off flux.³¹

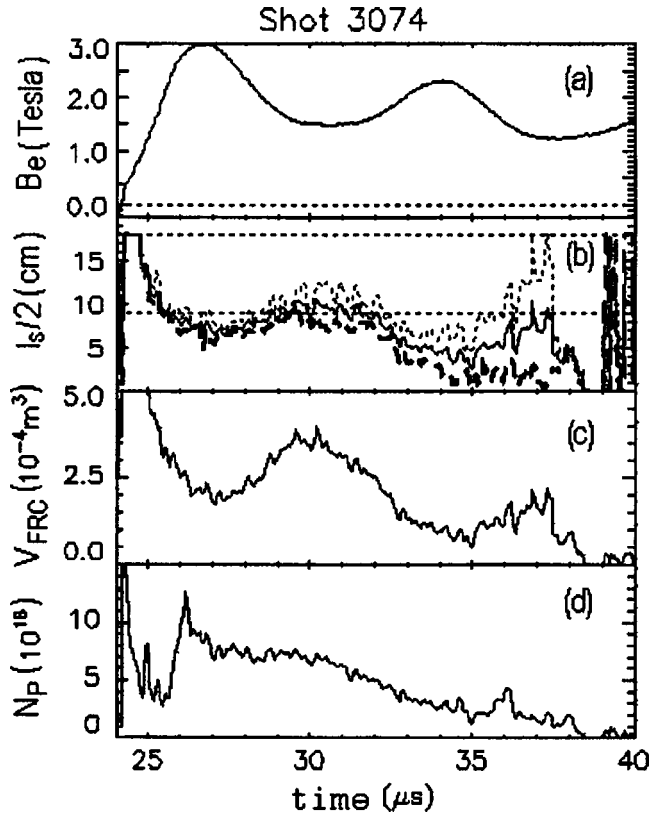


FIG. 4. Time histories of (a) external field measured at midplane; (b) half of separatrix length (solid line), west vertex of FRC separatrix volume from midplane (thin dashed line), and east vertex of FRC separatrix volume from midplane (thick dashed line); (c) FRC separatrix volume; and (d) FRC particle inventory.

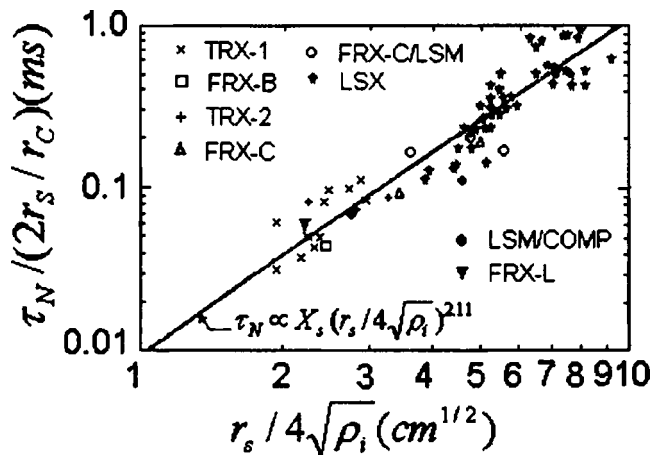


FIG. 5. Comparing particle confinement time τ_N of typical high-density FRC in FRX-L with previous experiments and empirical scaling. FRX-L τ_N obtained during 26.5–30.5 μ s immediately after formation is added in Fig. 8 of Ref. 12. The experiments are (\times , TRX-1, $r_c=12$ cm), (\square , FRX-B, $r_c=12.5$ cm), ($+$, TRX-2, $r_c=12.5$ cm), (Δ , FRX-C, $r_c=25$ cm), (\circ , FRX-C/LSM, $r_c=35$ cm), (\star , LSX, $r_c=45$ cm), (\bullet , LSM/COMP, $r_c=23$ cm), and (∇ , FRX-L, $r_c=6.29$ cm).

Another important formation related factor is $G_{LO} = B_{LO}/B_{GN}$, where B_{GN} is the Green–Newton field.⁹ G_{LO} is a heating related indication factor during FRC formation by FRTP method. Higher G_{LO} would allow more prominent resistive and axial contraction heating that favors our intention to produce a high-density FRC with adequate temperature.^{9,31} At 50 mTorr in FRX-L, $B_{GN} \approx 3.2$ kG and $G_{LO} \approx 0.5$. According to Tuszewski,³¹ the ratio of the total temperature T over zero-bias temperature limit T_l observes the scaling $T/T_l = (\sqrt{3}/2)(1 + 1.7G_{LO}^{1.5})^{-1} + 2.7G_{LO}^{1.2}$. The measured T/T_l in the typical shot is estimated as 2.7 if taking temperature data immediately after FRC formation, and $T/T_l \approx 1.4$ if using temperature at 30 μ s. These numbers show that FRX-L observes the scaling that was already verified by experimental results from FRX-series, TRX-series, and LSM experiments.³¹

The flux time history is similar to the particle inventory, as seen in the plot of FRC internal flux [Fig. 3(h)]. Applying an exponential fit to FRC internal flux, a flux confinement time $\tau_\Phi = -\Phi_P/(d\Phi_P/dt)$ is obtained.^{20,22} τ_Φ is about 20 μ s during 26.5–30.5 μ s and 6.7 μ s as the FRC is compressed again by external field. The values of τ_N and τ_Φ during 26.5–30.5 μ s are intrinsic to FRX-L FRC properties, and we expect they should apply to the entire FRC equilibrium when we considerably improve the crowbar switch operation in the near future.

D. Comparing FRX-L to FRC empirical scaling laws

Many attempts have been made to establish scaling laws or theoretical models to describe τ_N and τ_Φ .^{10,11,17,18,20,21,32} Using the τ_Φ scaling¹² of τ_Φ (ms) = $9X_s^{0.5}[r_s$ (m)/ $\times \sqrt{\rho_i}$ (cm)]^{2.14}, where ρ_i is ion gyroradius at external field,¹² the instantaneous τ_Φ are estimated as $\tau_\Phi(t=27 \mu\text{s})=28 \mu\text{s}$ and $\tau_\Phi(t=30 \mu\text{s})=30 \mu\text{s}$, respectively. The flux confinement time τ_Φ calculated from the scaling is 40% higher than the experimental data obtained immediately after the FRC is

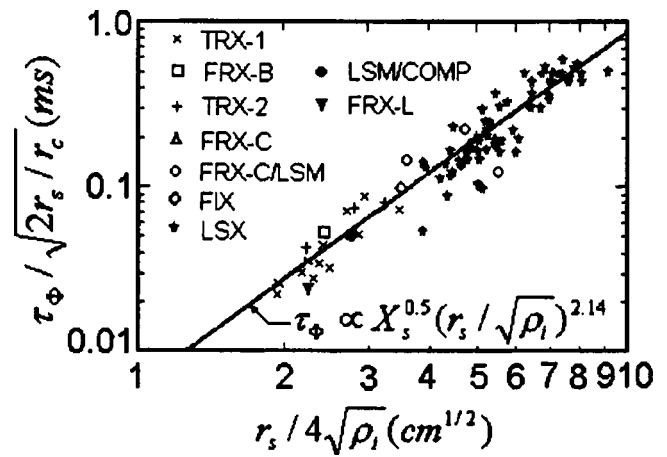


FIG. 6. Comparing flux confinement time τ_Φ of typical high-density FRC in FRX-L with previous experiments and empirical scaling. FRX-L τ_Φ obtained during 26.5–30.5 μ s immediately after formation is plotted in Fig. 6 of Ref. 12. The experiments are (\times , TRX-1, $r_c=12$ cm), (\square , FRX-B, $r_c=12.5$ cm), ($+$, TRX-2, $r_c=12.5$ cm), (Δ , FRX-C, $r_c=25$ cm), (\circ , FRX-C/LSM, $r_c=35$ cm), (\diamond , FIX, $r_c=40$ cm), (\star , LSX, $r_c=45$ cm), (\bullet , LSM/COMP, $r_c=23$ cm), and (∇ , FRX-L, $r_c=6.29$ cm).

formed and 4.5 times longer than τ_Φ from the middle of the equilibrium phase. Figure 6 compares τ_Φ obtained during 26.5–30.5 μ s with data from previous experiments and empirical scaling. The FRX-L data are plotted in Fig. 6 of Ref. 12. τ_Φ and τ_N scaling laws derived by Hoffman¹² approximately describe the FRX-L FRC's confinement times at 50 mTorr until FRC properties deteriorate due to external field modulation.

The major differences between scaling laws and experimental data in the middle of the equilibrium phase (when external field starts increasing) are due to the severe main field ringing. Figure 7 shows the excluded radius axial profile at 27 μ s and 30 μ s in the same shot as Fig. 3. The separatrix length is almost as long as the θ -coil length around $t=30 \mu\text{s}$. We suspect that the ringing caused rapid internal flux loss by opening the closed-field lines (poloidal flux) in the FRC when the FRC expanded axially and got close to the θ -coil ends, and particles that found themselves on open-field lines were rapidly lost. Here are the two proposed mechanisms that are responsible for the process. First, the FRC

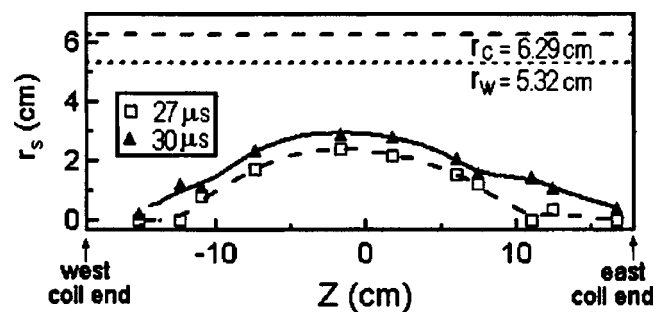


FIG. 7. Measured excluded flux radius axial profile at 27 μ s (the squares and dashed line) and at the middle of FRC equilibrium (30 μ s, the triangles and solid line). Markers on the line represent measurements from each probe location along axis; $z=0$ at midplane of θ -coil. The lines are spline interpolated to the measured data points.

TABLE III. Characteristic dimensions and collisional scale lengths of FRCs in FRX-L, FRX-B (Ref. 18), TRX-1 (Ref. 20), and LSX (Ref. 12) experiments.

Parameters	FRX-L	TRX-1	FRX-B	LSX
P_0 (mTorr)	50	20	17	2.5
r_c (cm)	6.29	12.5	12.5	45
r_s (cm)	2.9	2.7	5	15.8
λ_I (cm)	2.2	6.5	10	68
ρ_{gi} (cm)	0.09	0.3	0.3	0.5
r_s/ρ_{gi}	32	9	17	32
r_s/λ_I	1.3	0.4	0.5	0.2

experiences stronger interactions with neutral gas at its peripheries (separatrix) when the FRC moves towards the θ -coil ends. Second, the axial balanced equilibrium between the FRC and the open-field line magnetic pressure could not be maintained due to the suddenly reduced open-line field pressure at the θ -coil ends, the FRC must reduce its pressure by opening closed-field lines accordingly. These possibilities suggest that extending FRX-L θ -coil length should be helpful to confine FRCs better.

It is observed that $\tau_N \sim 2\tau_\Phi$ in the typical FRC in FRX-L. We suspect that the temperature profile and resistivity profile may not be uniform inside the separatrix radius, which differs from previous FRCs if it is true. Historically, most of the experimental data under 20 mTorr gave $\tau_N \sim \tau_\Phi$.^{22,12,33} The few attempts that actually measured FRC internal temperature profiles by Thomson scattering diagnostics also suggested an almost uniform temperature profile inside the FRC separatrix.^{18,34} With the assumption of flat temperature profile together with other assumptions, it is found that most resistivity profiles are approximately uniform in the FRCs with $\tau_N \sim \tau_\Phi$.^{20,21,33} However, the FRC in FRX-L is fairly collisional compared with previous experiments.²³ Table III lists characteristic dimensions and collisional scale lengths of FRCs in FRX-L, FRX-B,¹⁸ TRX-1,²⁰ and the LSX (Ref. 12) experiments. FRX-L is compact in size, but has the highest density and collisionality among all the experiments. As an example, taking FRX-L FRC data at 30 μ s, the ion mean free path $\lambda_I \sim 2.2$ cm, ion gyroradius at separatrix $\rho_{gi} \sim 0.09$ cm, the FRC separatrix radius $r_s \sim 2.9$ cm, and thus $r_s/\lambda_I \sim 1.3$, and $r_s/\rho_{gi} \sim 32$. It is conceivable that a nonuniform temperature profile may exist inside the separatrix enclosure in this relatively collisional FRC.

FRC energy confinement^{13,22} is not analyzed in this paper due to two reasons. First, the complexity of including the effects of FRC shape and volume changes during the external field modulation, which is severe in this case; second, the lack of independent measurements of FRC temperature time history and spatial profile. Without addressing these two issues, an FRC energy confinement analysis in FRX-L may not be meaningful to compare to empirical scaling.

E. FRC stability and stable time

FRCs in FRX-L have small s value between 1.5–1.7 that falls into the established FRC good confinement low s regime.^{13,20,22} However, neither experiments nor theoretical

stability analyses have defined the exact boundaries of FRC stable regimes. The typical FRX-L FRCs have $S^*/E \approx 5$ (or $s/E \approx 0.55$), where $S^* \approx 15$ ($s \approx 1.6$), $E \approx 2.9$ at time of 26.5 μ s, and $S^*/E \approx 3.4$ (or $s/E \approx 0.46$), where $S^* \approx 12$ ($s \approx 1.66$), $E \approx 3.6$ during the middle of equilibrium phase. These numbers put FRX-L FRCs into the margins of stability limits suggested by previous experiments^{35,36} and theories.^{24,25} Nevertheless, in Sec. IV, we will show that very good reproducibility can be achieved in forming such high-density FRCs in FRX-L.

The FRC stable time τ_s is of particular interest in FRX-L for the intention of using FRC as a target for MTF. Given the funding and time constraints in the current FRC-MTF program, as well as the obvious increased complexity in the possible system design, applying multipole fields³⁷ to suppress the $n=2$ instability in the FRC-MTF scheme is not investigated experimentally; therefore we are concerned how τ_s is related to other parameters as in the early days of FRC research.^{17,18,38} This is a topic that has not been addressed much since complete suppression of the $n=2$ instability by external multipole fields was demonstrated. As shown in Fig. 3(a) the FRC is usually terminated as the $n=2$ rotational instability grows. The stable time τ_s is about 8.5 μ s for the plasma shown in Fig. 3. The FRC lifetime is about 15.5 μ s determined from the excluded flux measurement [Fig. 3(g)] at the midplane ($z=0$).

From FRX-A and FRX-B data, Lipson¹⁷ formulated the scaling $\tau_s \approx 0.6R^2/\rho_i$ (μ s), where $R = \sqrt{2}/2r_s$ is the FRC major radius. This formula would lead to $\tau_s \approx 21$ μ s in the FRC shown in Fig. 3. As plasma spin-up is mostly caused by particle loss and end shorting, Tuszewski¹⁹ took into account the contributions of these two factors and proposed an empirical scaling law on τ_s to relate both the particle loss characteristic time τ_N and the end shorting parameters l_c/V_A , where l_c is the θ -coil length and V_A is the Alfvén velocity in the FRC open-field line. The derived scaling $1/\tau_s = 1/\tau_P + 1/\tau_v$, where τ_P and τ_v are proportional to τ_N and l_c/V_A , respectively, was claimed to be consistent with all then available FRC data. This scaling would give $\tau_s \approx 14$ –18 μ s in the typical FRX-L FRC based on the measured τ_N after axial contraction and in the middle of equilibrium. The measured $\tau_s \approx 8.5$ μ s in FRX-L is 2–2.5 times less than either of the predictions. Since the two formulas worked well with previous experimental data, and FRX-L τ_Φ and τ_N are in fairly good agreement with previous experiments, we would again ascribe the discrepancy to the main field modulation that causes abrupt confinement deterioration in the FRC equilibrium, as shown previously in the τ_Φ and τ_N analyses. Therefore, reducing the main field modulation and/or extending the length of the θ -coil will likely extend the good FRX-L confinement properties promptly after formation throughout the whole equilibrium phase.

IV. REPRODUCIBLE HIGH-DENSITY FRC PLASMAS IN FRX-L

An optimum parameter window that includes fill pressure, reversed bias field inside the θ -coil, impurity content in the preionization plasma, control of cusp locations at θ -coil

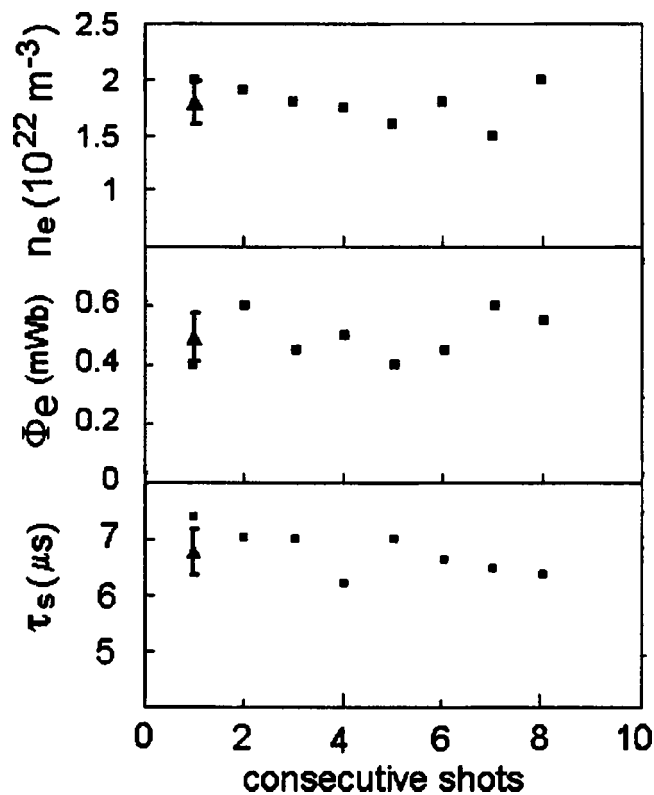


FIG. 8. Statistics on FRC average density during middle of FRC equilibrium (top), the estimated poloidal flux (middle), and the FRC stable time (bottom) in the trial set of consecutive eight discharges to reproduce high-density FRCs in FRX-L at 50 mTorr. Rectangles represent data in each shot; triangles are mean values over the shots. Error bars are standard deviations.

ends, and precise timing of initiating main external field to avoid asymmetries in preionization plasma has been identified in FRX-L. As a demonstration, eight consecutive shots were fired at the same engineered parameter settings in the parameter window to check how well FRX-L may reproduce key FRC parameters. Figure 8 (top) shows statistics of the volume density around $30 \mu\text{s}$ during the FRC equilibrium. The averaged density is $1.8 \times 10^{22} \text{ m}^{-3}$, with standard deviation in the mean of 7%. Figure 8 (middle) shows the statistics of trapped flux immediately after axial contraction, the average is 0.5 mWb, with standard deviation in the mean of 3%. Figure 8 (bottom) shows FRC stable time τ_s : $6.4\text{--}7.4 \mu\text{s}$, which has the largest variation among all parameters surveyed. The reason is that FRC stable times counted on the details of FRC evolution histories, and we know that the FRC confinement properties changed dramatically during the FRC equilibrium.

V. SUMMARY

Typical high-density FRC data in FRX-L are presented and analyzed. The FRCs have a density of $(2\text{--}4) \times 10^{22} \text{ m}^{-3}$, lifetime of $15\text{--}20 \mu\text{s}$, and total temperature of $300\text{--}500 \text{ eV}$. The achieved FRC density is within a factor of 2–3 from the desired density in the FRC-MTF scheme, the FRC stable time is half the desired value, and the total temperature is in the desired range for the MTF target plasma.

The FRCs are formed at 50 mTorr deuterium static fill at 2 kG net reversed bias field inside the θ -coil confinement region. During a set of consecutive discharges, major FRC parameters are shown to be within 10% deviations from their mean values. The data validated the extrapolation of previous scaling laws to the fairly collisional FRCs in FRX-L. However, it will be very important to watch for the development of possible growing discrepancies with empirical scaling laws as we explore even higher density FRCs.

Large differences exist in the FRC stable time, which is 2–2.5 times less than scaling. They are believed to be resulting from external main field modulation, which caused abrupt confinement deterioration due to opening trapped field lines in the FRC. Therefore, either reducing external field modulation considerably or extending the θ -coil length to accommodate FRCs inside the θ -coil will hopefully extend the good confinement properties which showed agreement with scaling laws to the rest of the FRC equilibrium phase. This could eventually lead to much longer FRC stable time and higher density during the equilibrium phase if the good confinement and transport properties will be retained in high-density regime.

Lack of independent temperature profile measurements prevents us from further understanding the nature of $\tau_N \sim 2\tau_\phi$, which is different from most previous experimental results of $\tau_N \sim \tau_\phi$. This could be a clue that shows differences in high-density collisional FRCs, and that fine structure of resistivity and temperature profiles may exist in very collisional FRCs. Fill pressure scans into higher density regimes at higher bias field levels are needed to further clarify these issues.

ACKNOWLEDGMENTS

It is a pleasure to acknowledge the technical help from Dr. A. L. Hoffman's FRC team in the University of Washington. The authors also would like to express their thanks to Dr. M. G. Tuszewski for his guidance in many ways. Timely technical support from E. M. Tejero, D. Begay, R. Aragonese, and E. Mignardot, is greatly appreciated.

This research was supported through the U. S. Department of Energy Contract No. W-7405-ENG-36 by the Office of Fusion Energy Sciences.

¹R. E. Siemon, R. I. Lindemuth, and K. F. Schoenberg, Comments Plasma Phys. Controlled Fusion **18**, 363 (1999).

²R. C. Kirkpatrick, I. R. Lindemuth, and M. S. Ward, Fusion Technol. **27**, 201 (1995).

³J. Wesson, *Tokamaks*, 3rd ed. (Clarendon, Oxford, 2004).

⁴J. Lindl, Phys. Plasmas **2**, 3933 (1995).

⁵I. R. Lindemuth, R. E. Reinovsky, R. E. Chrien *et al.*, Phys. Rev. Lett. **75**, 1953 (1995).

⁶A. J. Kemp, M. M. Basko, and J. Meyer-ter-vehn, Nucl. Fusion **43**, 16 (2003).

⁷G. A. Wurden, K. F. Schoenberg, R. E. Siemon *et al.*, J. Plasma Fusion Res. **2**, 238 (1999).

⁸J. M. Taccetti, T. P. Intrator, F. J. Wysocki, K. Forman, D. Gale, S. Coffey, and J. H. Degnan, Fusion Sci. Technol. **41**, 13 (2002).

⁹A. L. Hoffman, R. D. Milroy, J. T. Slough, and L. C. Steinhauer, Fusion Technol. **9**, 48 (1986).

¹⁰D. J. Rej, W. T. Armstrong, R. E. Chiren, P. L. Klingner, R. K. Linford, K. F. McKenna, E. G. Sherwood, R. E. Siemon, and M. Tuszewski, Phys. Fluids **29**, 852 (1986).

- ¹¹M. Tuszewski, Nucl. Fusion **28**, 2033 (1988).
- ¹²A. L. Hoffman and J. T. Slough, Nucl. Fusion **33**, 27 (1993).
- ¹³J. T. Slough and A. L. Hoffman, Phys. Fluids B **5**, 4366 (1993).
- ¹⁴S. Okada, T. Asai, F. Kodaera *et al.*, Nucl. Fusion **41**, 625 (2001).
- ¹⁵H. Y. Guo, A. L. Hoffman, R. D. Brooks, A. M. Peter, Z. A. Pietrzyk, S. J. Tobin, and G. R. Votroubek, Phys. Plasmas **9**, 185 (2002).
- ¹⁶M. Tuszewski, W. T. Armstrong, R. E. Chrien *et al.*, Phys. Fluids B **3**, 2844 (1991).
- ¹⁷J. Lipson, W. T. Armstrong, J. C. Cochrane, K. F. McKenna, E. G. Sherwood, and M. Tuszewski, Appl. Phys. Lett. **39**, 43 (1981).
- ¹⁸W. T. Armstrong, R. K. Linford, J. Lipson, D. A. Platts, and E. G. Sherwood, Phys. Fluids **24**, 2068 (1981).
- ¹⁹M. Tuszewski, G. A. Barnes, R. E. Chrien, W. N. Hugrass, D. J. Rej, R. E. Siemon, and B. Wright, Phys. Fluids **31**, 946 (1988).
- ²⁰J. T. Slough, A. L. Hoffman, R. D. Milroy, D. G. Harding, and L. C. Steinhauer, Nucl. Fusion **24**, 1537 (1984).
- ²¹L. C. Steinhauer, R. D. Milroy, and J. T. Slough, Phys. Fluids **28**, 888 (1985).
- ²²A. L. Hoffman and J. T. Slough, Nucl. Fusion **26**, 1693 (1986).
- ²³T. Intrator, S. Y. Zhang, J. H. Degnan *et al.*, Phys. Plasmas **11**, 2580 (2004).
- ²⁴A. Ishida, R. Kanno, and L. C. Steinhauer, Phys. Fluids B **4**, 1280 (1992).
- ²⁵H. Ji, M. Yamada, R. Kulsrud, N. Pomphrey, and H. Himura, Phys. Plasmas **5**, 3685 (1998).
- ²⁶J. M. Taccetti, T. P. Intrator, G. A. Wurden *et al.*, Rev. Sci. Instrum. **74**, 4314 (2003).
- ²⁷G. A. Wurden, T. P. Intrator, D. A. Clark *et al.*, Rev. Sci. Instrum. **72**, 552 (2001).
- ²⁸S. Y. Zhang, E. M. Tejero, J. M. Taccetti, G. A. Wurden, T. P. Intrator, W. J. Waganaar, and R. Perkins, Rev. Sci. Instrum. **75**, 4289 (2004).
- ²⁹M. Tuszewski and W. T. Armstrong, Rev. Sci. Instrum. **54**, 1611 (1983).
- ³⁰L. C. Steinhauer, Phys. Fluids **26**, 254 (1983).
- ³¹M. Tuszewski, Phys. Fluids **31**, 3754 (1988).
- ³²L. C. Steinhauer, Phys. Fluids **29**, 3379 (1986).
- ³³R. E. Chrien and S. Okada, Phys. Fluids **30**, 3574 (1987).
- ³⁴D. J. Rej and W. T. Armstrong, Nucl. Fusion **24**, 177 (1984).
- ³⁵M. Tuszewski, D. C. Barnes, R. E. Chrien, J. W. Cobb, D. J. Rej, R. E. Siemon, D. P. Taggart, and B. L. Wright, Phys. Rev. Lett. **66**, 711 (1991).
- ³⁶M. Tuszewski, D. P. Taggart, R. E. Chrien, D. J. Rej, R. E. Siemon, and B. L. Wright, Phys. Fluids B **3**, 2856 (1991).
- ³⁷S. Ohi, T. Minato, Y. Kawakami *et al.*, Phys. Rev. Lett. **51**, 1042 (1983).
- ³⁸L. C. Steinhauer, Phys. Fluids **24**, 328 (1981).